Chapter 7:
Recent Global CO$_2$ Scenario

This study looks into the feasibility of determining the seasonal variation of atmospheric carbon dioxide (CO_2) at global level based on the data procured by Orbiting Carbon Observatory-3 (OCO-3) the recent-most global CO_2 sensor. The uncalled for global lockdown related to the novel coronavirus (COVID-19) pandemic and the consequent restricted fossil fuel burning situation prevailed during the period of CO_2 data procurement. Keeping this factor into consideration, a comparative analysis with the predecessor Orbiting Carbon Observatory-2 (OCO-2) was carried out and a reduction in the CO_2 column average was found, especially in the urban regions. A wavelet coherence technique is suggested for quantifying the temporary reduction and it is envisaged that this technique would be beneficial in future comparisons of OCO-3 with its own yearly statistics.

7.1. Inspiration for the Work

As reviewed in Chapter 2, several space-borne, airborne, and ground-based sensing technologies have been developed during the last few decades for global CO_2 monitoring, together with the corresponding theoretical research, calibration, and validation. Orbiting Carbon Observatory-3 (OCO-3) (Eldering et al., 2019; Taylor et al., 2020) is the most recently introduced space-borne sensor launched (2019) by National Aeronautics and Space Administration (NASA) for monitoring atmospheric CO_2 at a global level. It is a newer version of its predecessor, Orbiting Carbon Observatory-2 (OCO-2) (Crisp et al., 2017; Eldering et al., 2017) and the spectrometric instrumentations are the same for the two sensors. Nevertheless, there are remarkable distinctions in respect of the global span, the observing platform and the mode of observations (Table 7.1).

Table 7. 1. Comparative view of the characteristics of OCO-2 and OCO-3 platforms.

Characteristics	OCO-2	OCO-3
Spectral channels	Centered on the molecular oxygen-A band (0.765 μm) and two CO$_2$ bands at 1.61 μm and 2.06 μm For solar induced fluorescence (SIF) 757 nm and 771 nm	Same as OCO-2
Orbit	near-polar, sun-synchronous orbit with a 1:36 PM ascending equator crossing time	external payload of the International Space Station, orbit repeat $\approx$ 3 days
Altitude	705 km	$\approx$ 410 km
Achieving nadir view	by tilting the instrument itself	through a mirror assembly
Sampling time	overpasses for a given latitude occur at the same local time of day	the overpass time is $\approx$ 20 min earlier each day, eventually sampling for diurnal variations of xCO$_2$ and SIF
Data procurement	September, 2014 to almost full 2020	August 2019 to mid-2022 (nominal lifetime)

The goal of this study is to investigate the applicability of OCO-3 data for calculating the yearly fluctuation of atmospheric CO$_2$, a well-known issue that has recently attracted fresh interest in India as well as worldwide. So it is obviously a matter of interest to justify the suitability of OCO-3 data for estimating the seasonal change of CO$_2$. Moreover, the circumstantial facts have given rise to the following candid questions.

- OCO-3 that began collecting scientific data in August 2019 has completed data procurement of two years without having any annual precedence of its own. Then what should be the reference to compare with at this moment?

- The unexpected pandemic situation prevailing during the last two years has inevitably curbed the worldwide fossil fuel burning. Has it imposed any obvious change in the atmospheric CO$_2$ composition?

- The more serious issue is that OCO-3 has completed more than half of its nominal

mission lifetime of three years with a major portion of year 2020 being within the worldwide restricted situation of fossil fuel burning. If that has actually distorted the normal CO$_2$ variation, then how to quantify the temporary deviation from the true picture?

Considering all these points, this work has carried out comparative analysis of column averaged dry air mole fraction of CO$_2$ (xCO$_2$) retrieved from OCO-3 and two related parameters, namely solar induced fluorescence (SIF) and dust aerosol optical depth (AOD) derived from both OCO-3 and OCO-2 database for nine urban and nine unpopulated regions of various global locations and have traced out the similarities and the dissimilarities in the trends of annual variation of these parameters. The OCO-2 records for the years 2018-20 are used as a reference. A wavelet transform approach is proposed for assessing the departure from the normal yearly xCO$_2$ fluctuation acquired from the OCO-3 database.

7.2. Data and Methodology

The vEarly global daily column averaged, bias corrected dry air CO$_2$ mole fraction (xCO$_2$) retrieved from OCO-3 were downloaded for the year 2020 from NASA's Goddard Earth Sciences Data and Information Services Center (GES-DISC) (https://disc.gsfc.nasa.gov). The corresponding SIF data, relevant to CO$_2$ uptake and the dust AOD data, supposed to be implicitly related to human activity were also taken into account. Also OCO-2 data (v10) for these three parameters were downloaded from the GES-DISC for three consecutive years 2018, 2019 and 2020. The following two data screening processes were implemented.

- For xCO$_2$, the good quality data were selected by using xCO$_2$ quality flag, which is '0' for L2 Lite file.
- For SIF, the missing values were taken care of by eliminating the data points with the flag of –9999.

7.2.1. Selection of xCO₂ Data and Fitting

Nine densely populated urban locations were selected randomly. Table 7.2 presents the detailed information on the selection process. A region of 2°×2° latitude-longitude span containing at least one large was selected within 10° bands of latitude ranging from 20° N to 50° N. Nine unpopulated places of the same 2°×2° span were selected between 50° N to 30° S (Table 7.2). These places were expected to be comprised of negligible human activities. Though the selections of urban and non-urban areas were arbitrary, only the zones having uniformly distributed OCO-2 and OCO-3 data throughout the year were considered. The xCO₂ and the related SIF values obtained from both OCO-2 and OCO-3 of the specified years were considered separately for each of these regions.

Table 7. 2. Locations of crowded urban and unpopulated natural regions selected around the globe, each of 2°×2° span

Latitude span	Urban (center)	Latitude span	Unpopulated (center)
20° N -30° N	Ahmedabad (23° N, 72.50° E) Bhopal (23.25° N, 77.35° E)	10° N-10° S	Congo Forest (7° N, 22° E) Atlantic Ocean-1 (8° S, 14° W) Pacific Ocean (10° S, 115° W)
30° N -40° N	Shanghai (31.23° N, 121.47°) Los Angeles (34.05° N, 118.24°W) Tokyo (35.67° N, 139.65° E) Beijing (40° N, 116° E)	10° N-50° N	Thar Desert (27° N, 71° E) Atlantic Ocean-2 (30° N, 45° W) Gobi Desert (43° N, 106° E)
40° N -50° N	New York (40.71° N, 74° W) Rome (41.90° N, 12.50° E) Paris (48.85° N, 2.35° E)	10° S -30° S	Yungas Foothills, Bolivia (14° S, 66° W) Campo Verde, Brazil (15° S, 55° W) Tanami Desert (21° S, 130° E)

The two major constraints faced in the work were (i) not getting sufficient daily data throughout the year and (ii) the limited matching period for available data of both OCO-3 and OCO-2. Though the orbiting platform has a well-defined repeat cycle that has not facilitated uniform data sampling for all the places. To accomplish with the existing resources, the OCO-3 time series data on xCO$_2$ and SIF for the year 2020 were compared with the same parameters of OCO-2 for year 2020 and the two preceding years 2018 and 2019.

The annual span of CO$_2$ variation is generally found to exhibit a single major periodic increase and decrease (Keeling et al., 1976; Basu et al., 2014). Such a variation can be fitted with polynomial (Raychaudhuri and Roy, 2020) or sinusoidal (Lindqvist et al., 2015) functions. Considering these features, the xCO$_2$ and SIF in the present case are expected to be normally distributed around the mean value and having irregular periodic increase and decrease. Such variations over three years were fitted with k-th order polynomial. The goodness of fit for n days or the minimization of residual error was decided by *Bayesian information criterion* (*BIC*) given by

$$BIC = n \ln \left[\frac{1}{n} \sum_{i=1}^{n} (y_i - \hat{y}_i)^2 \right] + k \ln(n) \tag{7.1}$$

In Eq. (7.1), the variables y_i and $\hat{y}_i$ represent the actual and the fitted value, respectively, for the i-th data point. The k corresponding to the minimum *BIC* value was considered as the proper order of the polynomial for fitting.

The following two parameters were defined in relation to the fitted curves for quantifying the observational inferences on the annual xCO$_2$ variation for each region.
Drop Time: It denotes the number of days between the xCO$_2$ extrema.
Slope: It is the ratio of the maximum-minimum xCO$_2$ difference to the corresponding difference of days.

7.2.2. Wavelet Analysis of the Seasonal CO$_2$

The interpretation of the seasonal CO$_2$ variation from OCO-3 data is a unique problem because it is a two-fold job. A reference is to be standardized for OCO-3 to compare with and both the spatial and temporal consistencies are to be taken care of. The former requirement is fulfilled with the fitted annual variations for a specific region derived from the database of its predecessor OCO-2 that had procured data before the commencement of the constrained fossil fuel burning situation. The latter requisite is achieved with the time-frequency decomposition of wavelet analysis technique introduced in Chapter 2.

In the present case, the spatial parameter is xCO$_2$ and the wavelet technique is implemented to its time-variation. The principle of working is to compare the time series with a standard, localized wave-like functional form called *wavelet* that has zero mean. This work has used Morlet waveform (plane wave modulated by Gaussian function) as the mother wavelet. The wavelet coherence analysis are conducted with two sets of time series: one is the OCO-2 data of 2019 and the other is the OCO-3 data of 2020 for each of the urban regions using Eq. (2.5). The objectives are to detect the existence of any possible localized consistency in phase and to identify any common patterns in the time and frequency intervals of the two time series.

As summarized in Chapter 2, the wavelet coherence is considered as the complex conjugate of the wavelet transforms of two signals named as wavelet cross spectrum which is normalized by the individual spectra and it identifies both the frequency band and the time interval where two time series are related. In the present case, the two time series are the annual changes of xCO$_2$ obtained from OCO-2, 2019 and OCO-3, 2020, respectively. The wavelet coherence is expected to point out the possible common patterns in the oscillating behaviour of these two and the phase arrow produces the visual representation of the phase difference between these two time series. To determine the presence of any probable localised consistency in phase, wavelet coherence analysis was performed for two sets of time series: OCO-2,'18, OCO-2,'19 plus OCO-3,'20 and OCO-2,'18, OCO-2,'19 plus OCO-2,'20 for each of the urban zones.

7.3. Results and Discussion

7.3.1. Variations in xCO$_2$ and SIF on an annual basis

Figure 7.1 and Figure 7.2 depict the seasonal fluctuations of kth order polynomial fitted xCO$_2$ at nine urban sites (Table 7.3) from 2018 to 2020 obtained from two different time series composite. Figure 7.1 consists of all OCO-2 data and Figure 7.2 contains OCO-2 for 2018 and 19 with OCO-3 for 2020. The symbols and fitting lines are as follows: 2018 square & red-solid, 2019 triangle & blue-dotted, and 2020 circle & black-dashed. The predicted feature of year-to-year secular rise in xCO$_2$ is noticeable in the majority of the locations depicted in both the Figure 7.1 and Figure 7.2. The xCO$_2$ begins in the year 2020 with a greater value than in 2018 and 2019, but begins to decrease earlier and at a faster rate in comparison to the prior years. Both OCO-2 and OCO-3 have been through the worldwide shutdown and the resulting reduction in fossil fuel emissions in 2020. This year's OCO-2 and OCO-3 data show a significant drop in xCO$_2$ for the majority of the locations in Figure 7.1 and 7.2. This points to a worldwide decline in the column average of CO$_2$ during the first half of 2020, notably after March.

Figure 7.3 summarizes the above findings by evaluating the *drop time* (*day*) and *slope* (*ppm/day*) for the xCO$_2$ yearly oscillations obtained from OCO-2, 2018 to 2020 (upper panels) and OCO-2, 2019 & 20 and OCO-3, 2020 (lower panels) for all of the metropolitan regions shown in Figure 7.1. It is worth noting that, in almost all situations, the slope has risen in 2020 compared to 2019, both for OCO-2 and OCO-3. This is the inverse of the natural trend of xCO$_2$ change from 2018 to 2019. The drop time also yields contradictory findings for 18-19 and 19-20. These findings suggest that xCO$_2$ levels in 2020 began to fall earlier and began to climb later than in prior years.
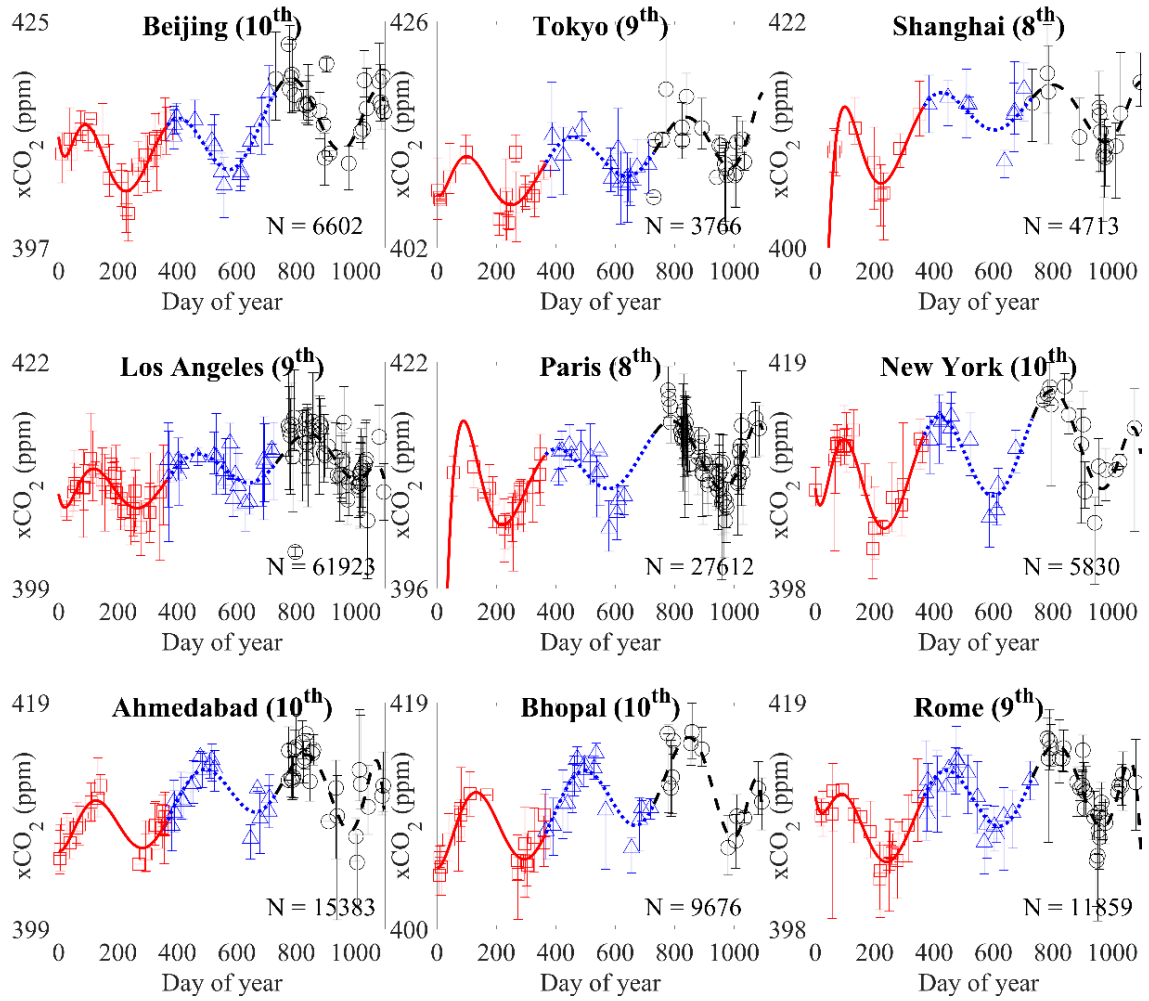
Figure 7. 1. Seasonal fluctuations in xCO_2 from 2018 to 2020 for the nine metropolitan areas (Table 7.3), computed from all OCO-2 measurements. Symbol with corresponding line: 2018 is a square with a red solid, 2019 is a triangle with a blue dot, and 2020 is a circle with a black dash. (N = the number of excellent data points discovered during a three-year period.)
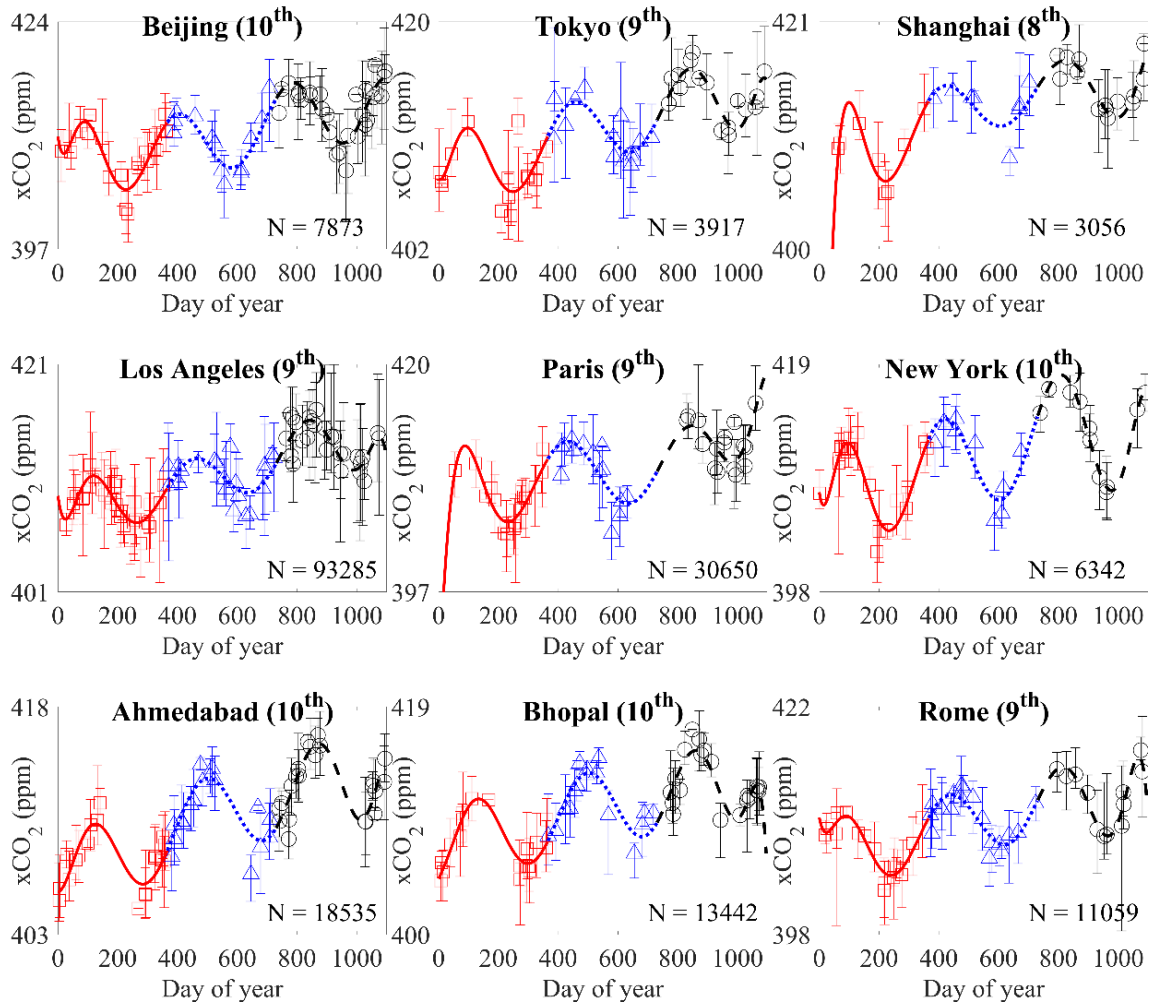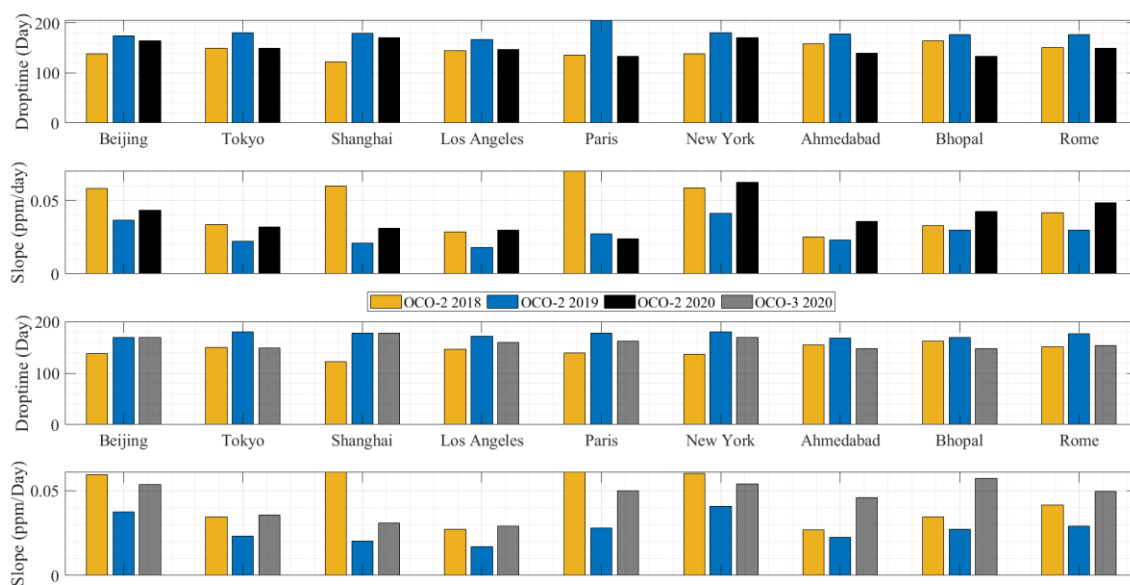
Figure 7. 2. Seasonal fluctuations in xCO_2 for the nine metropolitan areas (Table 7.3) from 2018 to 2020, calculated from OCO-2, 2018 & 19 with OCO-3, 2020. Symbol with corresponding line: 2018 is a square with a red solid, 2019 is a triangle with a blue dot, and 2020 is a circle with a black dash. (N = the number of excellent data points discovered during a three-year period.)

Figure 7. 3. Quantification of the *drop time* (*day*) and *slope* (*ppm/day*) for the xCO₂ yearly changes acquired from OCO-2, 2018 to 2020 (upper panels) and OCO-2, 2019 & 20 and OCO-3, 2020 (lower panels) for all of the metropolitan regions shown in Figure 7.1.

The plots of SIF ($Wm^{-2}nm^{-1}sr^{-1}$) produced solely from OCO-2 and that from both OCO-2 and OCO-3 for the same urban sites and fitted in the same manner with the same symbols as those in Figure 7.1 are shown in Figure 7.4 and 7.5 respectively. For both the cases in Figure 7.4 and 7.5, the seasonal patterns of SIF, a natural vegetative activity, show a typical rise in the middle of each year with no correlation to xCO₂. It implies that the unusual worldwide reduction in CO₂ column average during 2020 is due by man-made alterations rather than any divergence in natural carbon uptake.

Figure 7.6 depicts the xCO₂ fluctuations in areas devoid of human activity (Table 7.3), calculated from OCO-2 alone and Figure 7.7 a similar figure for OCO-2 and OCO-3 are displayed in the same way as Figure 7.1. For these areas, the findings are mixed. Parts of the Gobi Desert and the Atlantic Ocean, for example, show consistency with prior years' xCO₂ changes, including year-to-year increases, but parts of the Congo Forest and Thar Desert show quick decreases in xCO₂ comparable to those seen in Figure 7.1. The

opposing xCO_2 trend for southern hemisphere locales may also be seen. In general, the xCO_2 divergence in 2020 is significantly less pronounced in remote, unpopulated areas.
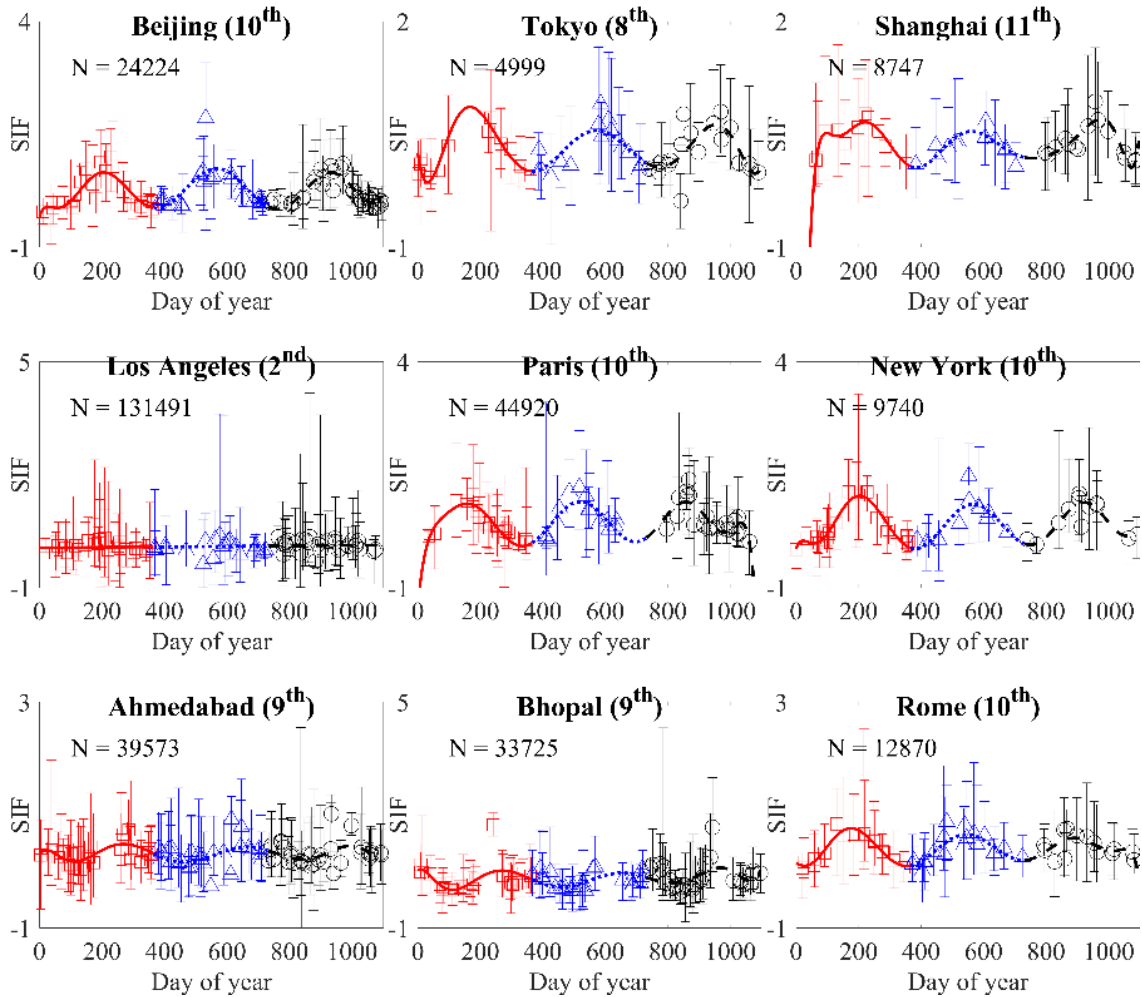

Figure 7. 4. Seasonal fluctuations in SIF $(Wm^{-2}nm^{-1}sr^{-1})$ from 2018 to 2020 for the nine metropolitan areas (Table 7.3), based on OCO-2, 2018, 19, and 20. Symbol and fitting line are the same as in Figure 7.1.
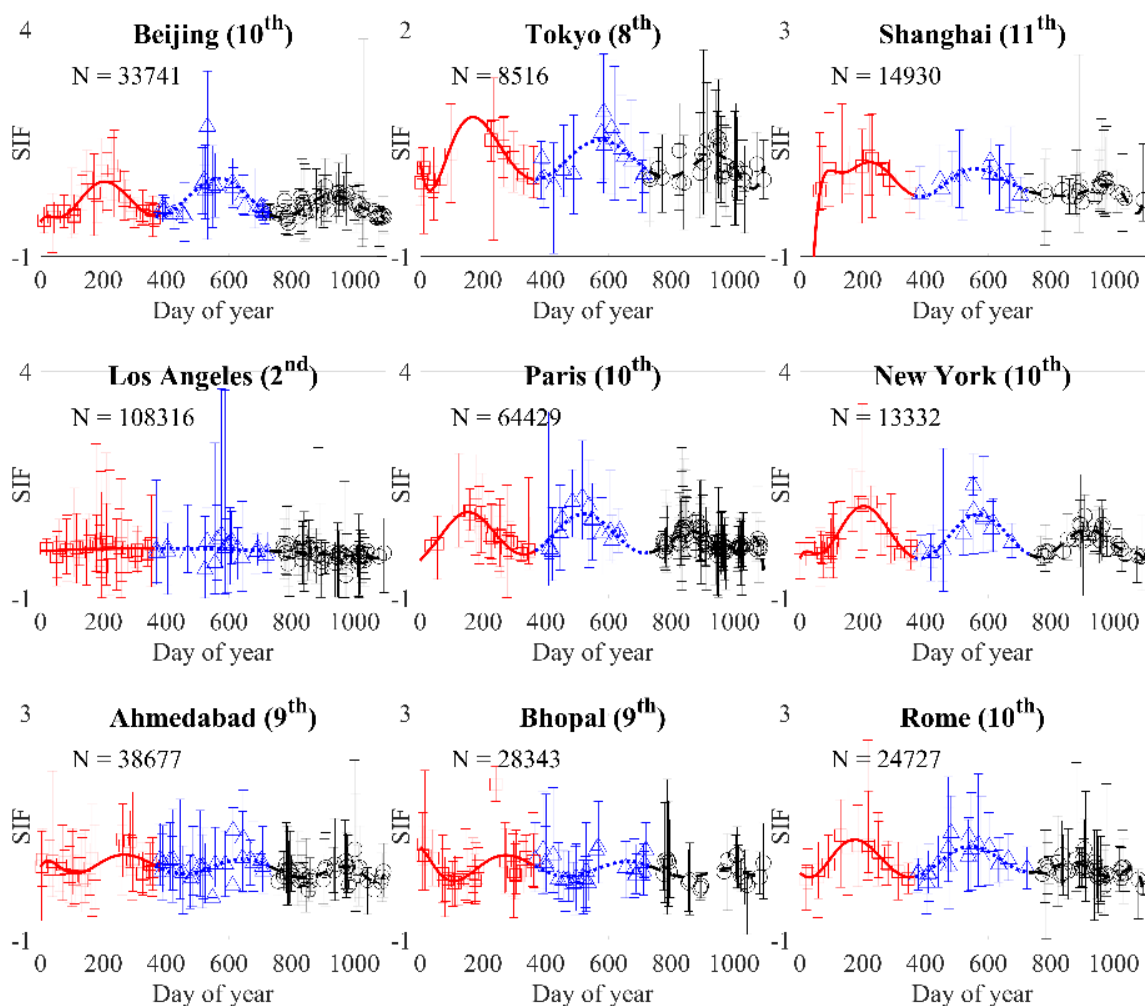
Figure 7. 5. Seasonal fluctuations in SIF ($Wm^{-2}nm^{-1}sr^{-1}$) from 2018 to 2020 for nine metropolitan areas (Table 7.3), calculated from OCO-2, 2018 & 19, and OCO-3, 2020. Symbol and fitting line are the same as in Figure 7.1.
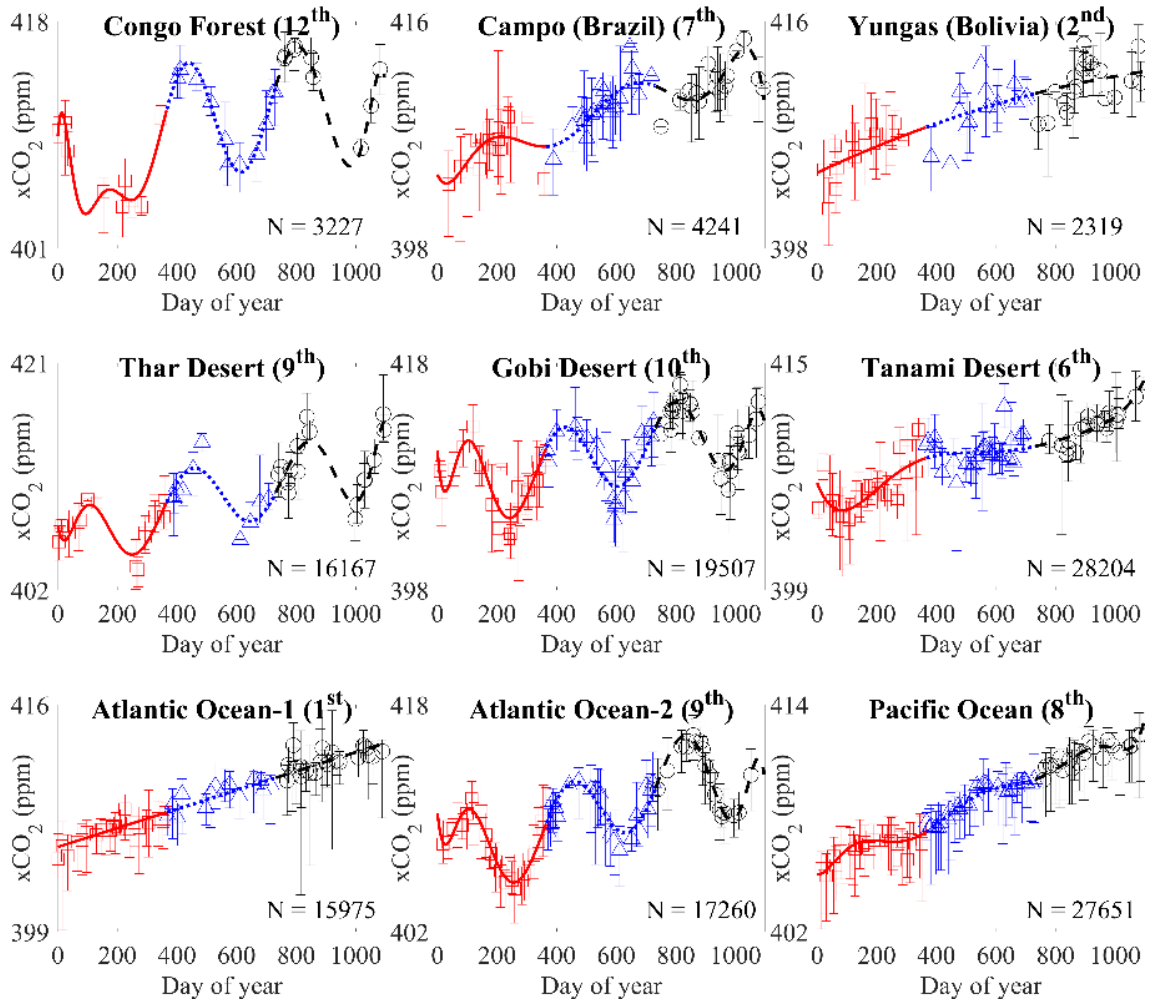
Figure 7. 6. Seasonal fluctuations in xCO_2 from 2018 to 2020 for nine unpopulated locations (Table 7.3), determined from OCO-2, 2018, 19, and 20. Symbol and fitting line are the same as in Figure 7.1.
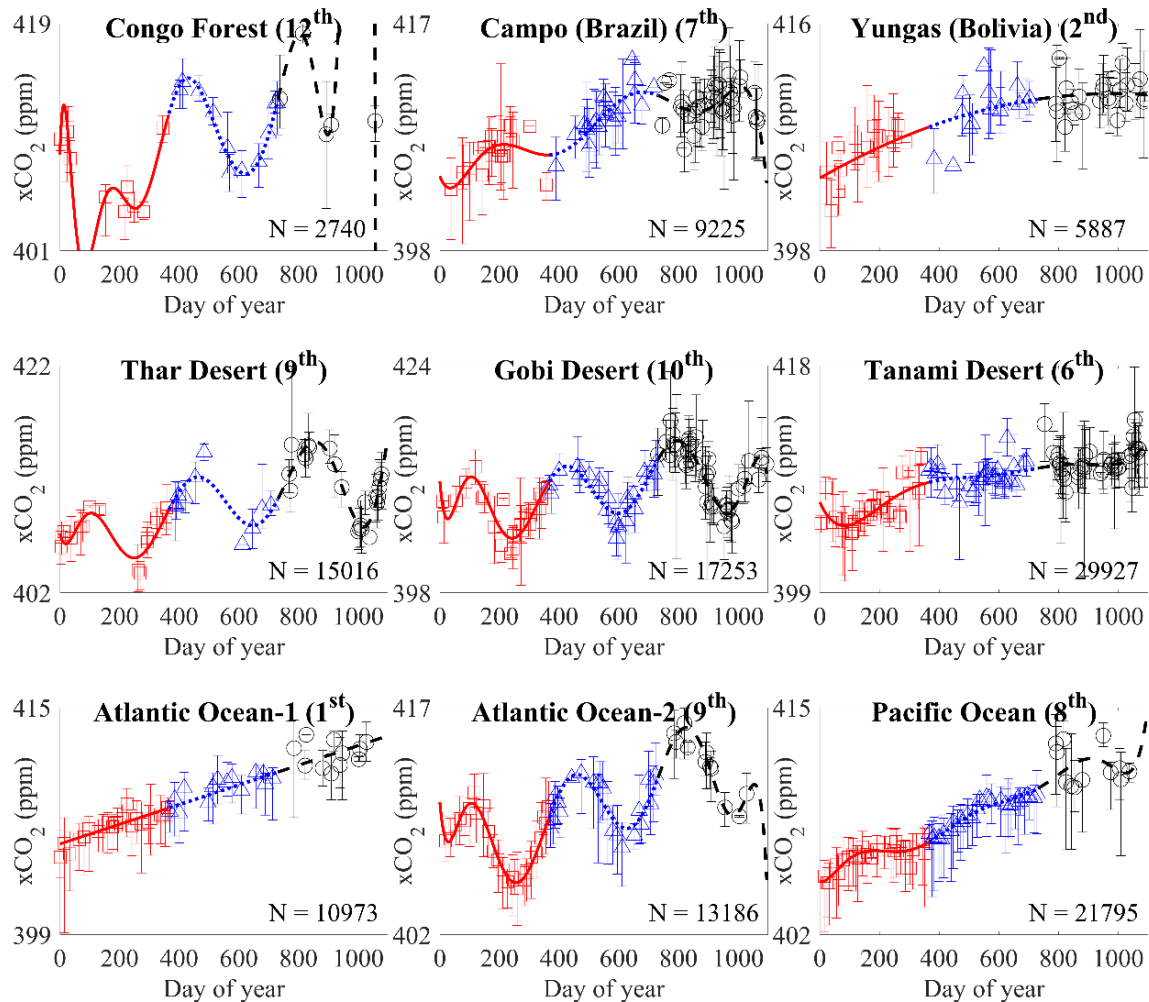
Figure 7. 7. Seasonal fluctuations in xCO$_2$ from 2018 to 2020 for nine unpopulated areas (Table 7.3), calculated from OCO-2, 2018 & 19, and OCO-3, 2020. Symbol and fitting line are the same as in Figure 7.1.

The observations above suggest that the dramatic decrease in global human activity of fossil fuel burning over the previous year has been mirrored globally, strongly or weakly at different locations, in the atmospheric CO$_2$ column average. The scenario has altered the typically expected seasonal variation of xCO$_2$, necessitating the quantification of the deviation from the real trend of CO$_2$ fluctuation obtained from OCO-3. The wavelet analysis is proposed for this aim, with the OCO-2 data from 2019 as a reference.

7.3.2. CO₂ Deviation in OCO-3 from Wavelet Analysis

As seen above, the reduction in atmospheric CO_2 caused by worldwide restrictions on the use of fossil fuels during the year 2020 has been included into the xCO_2 estimates provided by both OCO-2 and OCO-3 for the entire year. To quantify the departure from the typical seasonal fluctuation, the annual xCO_2 received from OCO-2 for the year 2019, cut out from Figure 7.2, was used as a reference, and wavelet coherence was performed using similarly cut out annual xCO_2 obtained from OCO-3 in the year 2020. The same procedure was conducted for all OCO-2 case cutting out the OCO-2 data for the year 2019 and 2020.

For any localised phase consistency, each zone was evaluated individually. Figure 7.8 depicts one such occurrence (Los Angeles). The majority of the figure, as indicated by the colour bar, shows nearly 100% coherency of the xCO_2 of both years (OCO-2, 2019 and OCO-3, 2020) during the whole time. The matching phase arrows indicate whether these are in phase or anti-phase. As illustrated by the phase arrows, certain localised phase changes occur inside the triangle mid-region (white shaded) with both time and frequency.

Figure 7.9 shows a realistic estimate of the phase difference for all urban regions and compares it to the drop time difference obtained from the fitted xCO_2 curves for the urban places (abbreviated) in the same order as in Figure 7.3. The span of phase change produced from wavelet coherence is well compatible with the drop time difference of the fitted curve, as shown in Figure 7.9. As a result, the phase difference of the yearly xCO_2 variation acquired from OCO-3, 2020 may be estimated as a measure of departure from the variation obtained in a normal condition, with OCO-2, 2019 serving as a proxy for the moment. The wavelet coherence approach is therefore demonstrated in this study as a tool for assessing the unexpected deviation from the regular yearly xCO_2 fluctuation acquired from the OCO-3 database using the matching OCO-2 data as a reference. In the future, a similar mechanism can be used with OCO-3 data obtained in tentatively normal conditions.
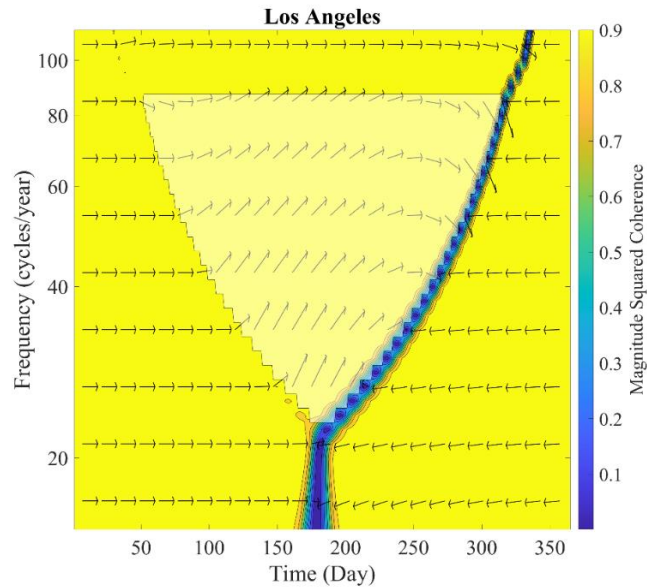
Figure 7. 8. An example of wavelet coherence of the xCO$_2$ yearly fluctuation obtained from OCO-2, 2019 and OCO-3, 2020 (Los Angeles).
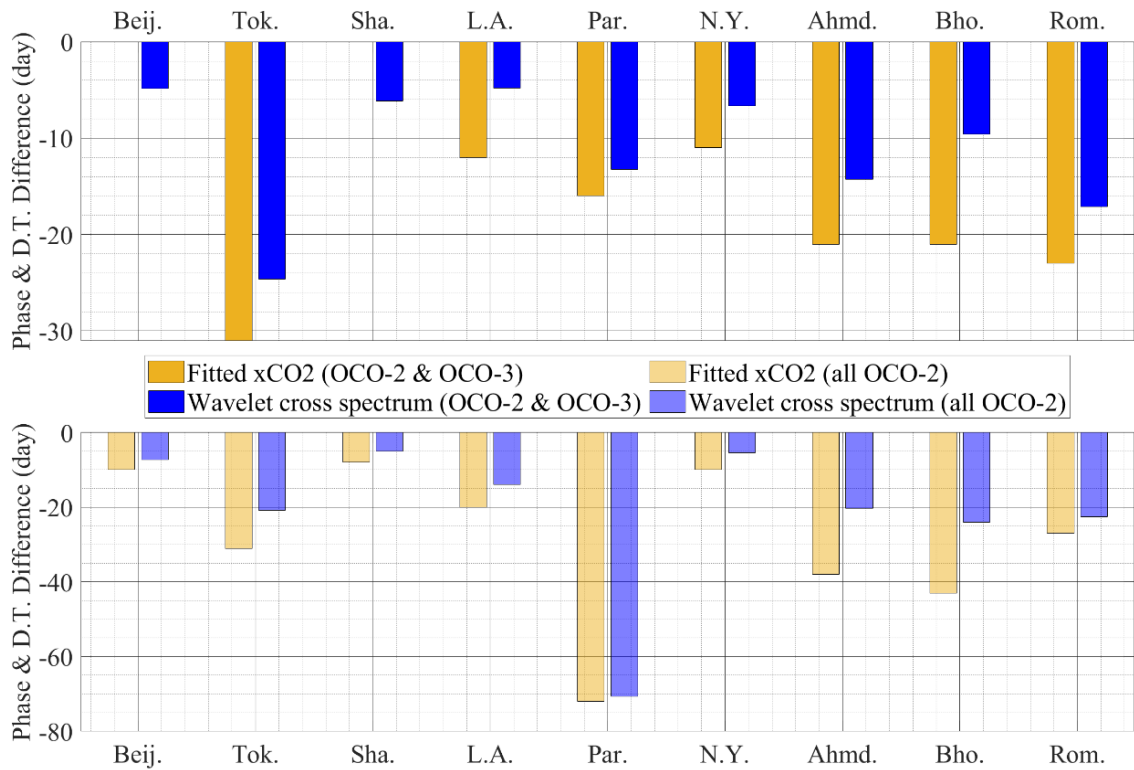

Figure 7. 9. Comparison of the wavelet phase difference and drop time differences of the fitted xCO$_2$ curves of (i) OCO-2, 2019 and OCO-3 2020 (top) and (ii) OCO-2, 2019 and OCO-2 2020 (bottom) for the urban locations abbreviated in the same order as in Figure 7.3.

161

7.3.3. AOD

The AOD-dust parameter, another component linked to human activity confinement, was also investigated. Because no regular yearly change in AOD was predicted, no fitting was attempted, and only discrete values were shown. There was no discernible anthropogenic change in the year 2020. The only noteworthy conclusions were that the quantity of optical depth measured by OCO-3 was often substantially lower than that obtained by OCO-2. A similar cyclical change in dust aerosol was also observed in two successive years. Aerosols in unpopulated areas were thought to be less connected to anthropogenic activity and were thus excluded.

7.4. Inferences

OCO-3 has a planned operational duration of three years, and because to the pandemic state, an unanticipated scenario of restricted human activity has evolved by this time. Given the likelihood of global fossil fuel constraints impacting the CO$_2$ column, the current study validates the applicability of OCO-3 data for tracking the relevant yearly change in CO$_2$ column average. A comparison study is done with its predecessor OCO-2 for the obtained data on xCO$_2$ and SIF in both urban and unpopulated areas across the world. During the first half of the year 2020, a notable fall in CO$_2$ column average was seen, notably in metropolitan areas, indicating a clear association with the sudden decline in global human activity. A wavelet coherence analysis approach is proposed for calculating the transitory decrease in CO$_2$ column average utilising 2019 OCO-2 data as a reference. In future, a similar approach may be applied to OCO-3 data obtained in normal air circumstances, which is likely to provide more accurate findings in the self-comparison.

The prime goal was to differentiate between the presence and absence of human activity. In contrast to heavily populated metropolitan areas, forests, seas, and deserts were chosen. For these locations, OCO-2 and OCO-3 obtained findings are elaborated. SIF variations throughout the same time period are also shown. Among so many results, an agreement has been formed that a significant fall in the atmospheric CO$_2$ column has

occurred globally, which is not a natural event but is the consequence of a sudden change in human activity. Other than the worldwide shutdown, there is no such noteworthy incident. In Figure 7.3, the trend of change in xCO$_2$ variation is assessed for both OCO-2 and OCO-3. Wavelet coherence (Figure 7.8 and 7.9) is a more precise approach that can determine the localised deviation in both time (day of year) and frequency (cycles per year).

Chapter References

Basu, S., Krol, M., Butz, A., Clerbaux, C., Sawa, Y. & Machida, T. et al. (2014). The seasonal variation of the CO2 flux over Tropical Asia estimated from GOSAT, CONTRAIL, and IASI. *Geophysical Research Letters*, 41(5), 1809-1815. doi: 10.1002/2013gl059105

Crisp, D., Pollock, H. R., Rosenberg, R., Chapsky, L., Lee, R. A. M. & Oyafuso, F. A. et al. (2017). The on-orbit performance of the Orbiting Carbon Observatory-2 (OCO-2) instrument and its radiometrically calibrated products. *Atmospheric Measurement Techniques*, 10(1), 59-81. doi: 10.5194/amt-10-59-2017

Eldering, A., Taylor, T. E., O'Dell, C. W. & Pavlick, R. (2019). The OCO-3 mission: measurement objectives and expected performance based on 1 year of simulated data. *Atmospheric Measurement Techniques*, 12(4), 2341-2370. doi: 10.5194/amt-12-2341-2019

Eldering, A., Wennberg, P. O., Crisp, D., Schimel, D. S., Gunson, M. R. & Chatterjee, A. et al. (2017). The Orbiting Carbon Observatory-2 early science investigations of regional carbon dioxide fluxes. *Science*, 358(6360), doi: 10.1126/science.aam5745

Keeling, C., Bacastow, R., Bainbridge, A., Ekdahl, C., Guenther, P., Waterman, L., & Chin, J. (1976). Atmospheric carbon dioxide variations at Mauna Loa Observatory, Hawaii. *Tellus*, 28(6), 538-551. doi: 10.1111/j.2153-3490.1976.tb00701.x

Lindqvist, H., O'Dell, C. W., Basu, S., Boesch, H., Chevallier, F. & Deutscher, N. et al. (2015). Does GOSAT capture the true seasonal cycle of carbon dioxide? *Atmospheric Chemistry and Physics*, 15(22), 13023-13040. doi: 10.5194/acp-15-13023-2015

Raychaudhuri, B. & Roy, S. (2020). Investigation of seasonal variability of atmospheric columnar CO$_2$ over India in relation to environmental parameters using OCO-2 observation and vertical redistribution model. *International Journal of Remote Sensing*, 42(4), 1450-1473. doi: 10.1080/01431161.2020.1832281

Taylor, T. E., Eldering, A., Merrelli, A., Kiel, M., Somkuti, P. & Cheng, C. et al. (2020). OCO-3 early mission operations and initial (vEarly) XCO$_2$ and SIF retrievals. *Remote Sensing of Environment*, 251, 112032. doi: 10.1016/j.rse.2020.112032